Frequency-Domain Design of a Reset-Based Filter: An Add-On Nonlinear Filter for Industrial Motion Control

S. Ali Hosseini, Fabian R. Quinten, Luke F. van Eijk, Dragan Kostić, and S. Hassan HosseinNia, *Senior Member, IEEE*

***Abstract*—This study introduces a modified version of the constant-in-gain, lead-in-phase (CgLp) filter, which incorporates a feedthrough term in the first-order reset element (FORE) to reduce the undesirable nonlinearities and achieve an almost constant gain across all frequencies. A backward calculation approach is proposed to derive the additional parameter introduced by the feedthrough term, enabling designers to easily tune the filter to generate the required phase. This article also presents an add-on filter structure that can enhance the performance of an existing LTI controller without altering its robustness margins. A sensitivity improvement indicator is proposed to guide the tuning process, enabling designers to visualize the improvements in closed-loop performance. The proposed methodology is demonstrated through a case study of an industrial wire bonder machine, showcasing its effectiveness in addressing low-frequency vibrations and improving overall control performance.**

***Index Terms*—Frequency-domain control design, linear-time-invariant (LTI) control limitations, precision motion control, reset control systems (RCSs).**

I. Introduction

LINEAR-TIME-INVARIANT (LTI) controllers are among the most commonly used controllers in industrial applications. Their popularity stems from their ease of tuning and implementation, as well as their ability to be represented in the frequency domain for both open- and closed-loop configurations. This characteristic is particularly advantageous because it eliminates the need for a parametric model of the system; instead, the design and tuning can be performed using only the measured frequency response function (FRF) of the system.

Received 31 March 2025; revised 22 September 2025; accepted 1 December 2025. Date of publication 19 December 2025; date of current version 25 February 2026. This work was supported by ASMPT and Holland High Tech, Topsector High Tech Systems and Materials, through the Public-Privat-Collaboration (PPS) Innovation Grant Public-Private Collaboration for Research and Development. Recommended by Associate Editor J. T. Gravdahl. *(Corresponding author: S. Ali Hosseini.)*

S. Ali Hosseini, Fabian R. Quinten, and S. Hassan HosseinNia are with the Department of Precision and Microsystems Engineering, Delft University of Technology, 2628 CD Delft, The Netherlands (e-mail: S.A.Hosseini@tudelft.nl; fabianrobertquinten@gmail.com; S.H.HosseinNiaKani@tudelft.nl).

Luke F. van Eijk is with ASMPT, 6641 TL Beuningen, The Netherlands, and also with the Department of Precision and Microsystems Engineering, Delft University of Technology, 2628 CD Delft, The Netherlands (e-mail: luke.van.eijk@asmpt.com).

Dragan Kostić is with ASMPT, 6641 TL Beuningen, The Netherlands (e-mail: dragan.kostic@asmpt.com).

Digital Object Identifier 10.1109/TCST.2025.3641635

In precision positioning platforms, there is a demand for extremely fast and accurate motions, which necessitates pushing controllers to their performance limits. However, LTI controllers face inherent limitations that prevent precision positioning systems from achieving the required levels of speed and accuracy. Bode's gain–phase relationship [1], and waterbed effect [2] are two well-known limitations of LTI control systems.

Over the years, various nonlinear and hybrid control strategies have been proposed to address these limitations, such as variable-gain integrators [3], hybrid integrator-gain systems [4], [5], and reset control systems (RCSs) [6], [7]. Among these approaches, RCSs have demonstrated significant potential for integration into precision motion control systems. Numerous studies have shown that these systems can overcome the limitations of LTI controllers [8], [9]. Moreover, one of the main reasons reset control is often preferred over other nonlinear filtering approaches is that, while its open-loop response can be analyzed in the frequency domain using the describing function (DF) method [10], it also uniquely offers analytical tools for closed-loop frequency-domain analysis [11], [12]. Specifically, [13] introduced higher order sinusoidal-input DFs (HOSIDFs) for open-loop RCSs, while [11], [14] introduced the closed-loop HOSIDF for such systems. Building on these results, [12] presents a sensitivity-like function, termed "pseudo-sensitivity," that facilitates closed-loop analysis of RCSs.

The concept of reset control was first introduced in [15] as a nonlinear integrator, later termed the Clegg integrator (CI). Over time, more sophisticated reset elements were developed, including the first-order reset element (FORE) [16], generalized FORE (GFORE) [8], and the second-order reset element (SORE) [17].

In [18], a reset-based filter, the constant-in-gain, lead-in-phase (CgLp) element, was introduced. By combining a GFORE element with a lead filter, this design provides broadband phase lead while maintaining an almost constant gain in its DF. Typically, the CgLp filter is employed to introduce a positive phase near the bandwidth frequency, thereby flexing the limitations imposed by Bode's gain–phase relationship. However, in the CgLp filter, the nonlinear integrator action persists at all frequencies (after the cutoff frequency of the GFORE element) due to the presence of the GFORE element.

This results in undesirable nonlinearities at frequencies where such behavior is unnecessary. Moreover, the filter exhibits an inherent low-pass characteristic at high frequencies, which contradicts its intended function of maintaining an almost constant gain. To address these challenges, this study proposes the following.

1) Modifying the existing CgLp element by incorporating the feedthrough term in the GFORE element, resulting in a new CgLp element with an almost constant 0-dB gain at all frequencies while exhibiting a reduced ratio of higher order harmonics to the first harmonic.

As noted, the feedthrough term of the GFORE element in this modified CgLp filter is not zero, introducing an additional parameter to be tuned compared to the original CgLp element. This additional parameter increases the complexity of the design process. Furthermore, since the CgLp filter is primarily a phase generator filter, the required phase is typically predefined in many applications, necessitating the tuning of the filter's parameters to achieve the desired phase. The inclusion of this extra parameter further complicates the tuning process. To address this issue, this study proposes the following.

1) An analytical backward calculation approach that derives the additional parameter of the modified CgLp filter from the required phase. This method provides a direct relationship between the CgLp parameters and the phase it generates, enabling designers to achieve the exact desired phase without added complexity.

This article examines an industrial wire bonder machine as a case study. This machine establishes physical connections between chips and their packaging, necessitating fast and precise motion. Its primary challenge stems from low-frequency base-frame vibrations, which require an increase in controller gain at low frequencies to mitigate positioning errors. However, due to Bode's gain–phase relationship and the waterbed effect, increasing gain can reduce the phase margin or violate robustness margins (e.g., the peak of the sensitivity function). Thus, the objective is to design a filter that increases gain at low frequencies without compromising robustness margins.

As noted, most industrial applications rely on LTI controllers, with a strong preference for preserving their characteristics while ensuring sufficient performance. Therefore, to further enhance system performance, it is essential to develop an architecture that functions as an add-on filter within existing control loops, eliminating the need for modifications to the implemented linear controller. To address these objectives, this study introduces the following.

1) The design of an add-on filter structure, along with step-by-step tuning guidelines, to enable performance improvement for any linear control system without altering the existing linear controller. Additionally, we propose a sensitivity improvement indicator that allows designers to directly shape and tune the nonlinear controller in closed-loop with respect to sensitivity improvements compared to the linear controller.

The remainder of this article is structured as follows. Section II introduces the reset element in the time domain.

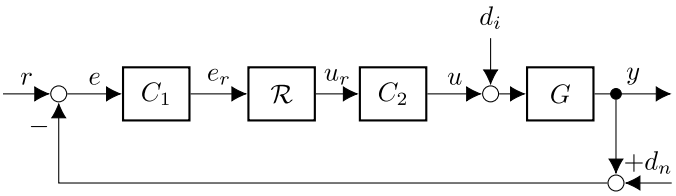

Fig. 1. Block diagram of the closed-loop system.

It then presents the open- and closed-loop frequency-domain representations of the RCS. In Section III, we modify the CgLp element by incorporating a proportional GFORE element and examine the effect of this modification on the influence of higher order harmonics. Additionally, we establish the relationship between the CgLp parameters and the required phase, enabling the filter to be designed independently of the added feedthrough term (thereby avoiding unnecessary complexity). In Section IV, we introduce the wire bonder machine as the case study and highlight the limitations of linear control and existing challenges. Subsequently, in Section V, we present the design and tuning method for a reset-based add-on filter that addresses the challenges observed in the LTI control of the wire bonder while also providing a general design and tuning method applicable to other systems. Additionally, we introduce the sensitivity improvement indicator, a frequency-domain-based method that visualizes the closed-loop performance comparison and prediction between the linear and reset-based controllers. In Section VI, we validate the findings of this study through experiments conducted on the industrial wire bonder machine. Finally, conclusions and suggestions for future work are provided in Section VII.

II. Reset Control Preliminaries

This section covers the fundamentals of reset control, including reset element definition and frequency-domain analysis for both open- and closed-loop RCSs.

A. Reset Element

Consider a closed-loop control system, as depicted in Fig. 1, where $(r(t), d_i(t), d_n(t)) \in \mathbb{R}$ represent the exogenous inputs, $u(t) \in \mathbb{R}$ is the control input, and $y(t) \in \mathbb{R}$ denotes the controlled output, all at $t \in \mathbb{R}_{\geq 0}$. The LTI plant is represented by G, while C_1 and C_2 are LTI filters. The reset element is denoted by $\mathcal{R}$ and is defined as follows:

$$\mathcal{R}: \begin{cases} \dot{x}_r(t) = A_r x_r(t) + B_r e_r(t), & \text{if } (x_r(t), e_r(t)) \notin \mathcal{F}, \\ x_r(t^+) = A_\rho x_r(t), & \text{if } (x_r(t), e_r(t)) \in \mathcal{F}, \\ u_r(t) = C_r x_r(t) + D_r e_r(t) \end{cases} \quad (1)$$

where the reset surface $\mathcal{F}$ is given by

$$\mathcal{F} := \{e_r(t) = 0 \wedge (A_\rho - I) x_r(t) \neq 0\} \quad (2)$$

with states $x_r(t) \in \mathbb{R}^{n_r \times 1}$, and after reset states $x_r(t^+) \in \mathbb{R}^{n_r \times 1}$. The state-space matrices of the reset element are given by $A_r \in \mathbb{R}^{n_r \times n_r}$, $B_r \in \mathbb{R}^{n_r \times 1}$, $C_r \in \mathbb{R}^{1 \times n_r}$, and $D_r \in \mathbb{R}$. The reset value matrix is denoted as $A_\rho = \text{diag}(\gamma_1, \ldots, \gamma_{n_r})$, where $-1 < \gamma_i < 1 \ \forall i \in \mathbb{N}$. $e_r(t) \in \mathbb{R}$ and $u_r(t) \in \mathbb{R}$ represent the

input and output of the reset element, respectively. A reset element follows its base linear system (BLS) dynamics if no reset happens ($(x_r(t), e_r(t)) \notin \mathcal{F}\ \forall\ t \in \mathbb{R}_{\geq 0}$). Thus, the transfer function of its BLS is defined as follows:

$$R(s) = C_r (sI - A_r)^{-1} B_r + D_r \tag{3}$$

where $s \in \mathbb{C}$ is the Laplace variable.

B. Open-Loop Frequency-Domain Analysis of RCSs

The nonlinear nature of reset elements presents significant challenges in designing controllers within the frequency domain, particularly when employing the widely used loop-shaping technique, which relies on Bode plots. Among the few methods available to estimate nonlinear controllers in the frequency domain, the DF method stands out. The DF characterizes the steady-state response of a convergent nonlinear system by representing it through the first harmonic component of the Fourier series expansion. In [8], the DF method is utilized to represent the reset element in the frequency domain. Building upon this, [11] introduced the extension of the frequency-domain tool known as HOSIDFs for reset controllers, enabling a more comprehensive open-loop analysis. Thus, having the input of the open loop as $e(t) = \hat{e}\sin(\omega t)$, the output $y(t)$ (while the loop is not closed) can be described by the Fourier series

$$y(t) = \sum_{n=1}^{\infty} |\mathcal{L}_n(j\omega)|\, \hat{e} \sin(n\omega t + \angle \mathcal{L}_n(j\omega)) \tag{4}$$

with $n \in \mathbb{N}$, and $\mathcal{L}_n(j\omega)$ is given as follows (see [9], [13]):

$$\mathcal{L}_n(j\omega) = G(nj\omega)\, C_2(nj\omega)\, H_n(\omega)\, C_1(j\omega)\, e^{j(n-1)\angle C_1(j\omega)}. \tag{5}$$

$H_n(\omega)$ is the HOSIDF of the reset element $\mathcal{R}$, which is introduced in [11] as the following theorem.

Theorem 1 [11, Th. 3.1]: The HOSIDFs of the reset element in (1) are expressed as follows:

$$H_n(\omega) = \begin{cases} C_r(j\omega I - A_r)^{-1}(I + j\Theta_D(\omega))\, B_r + D_r, \\ \text{for } n = 1 \\ C_r(jn\omega I - A_r)^{-1}\, j\Theta_D(\omega)\, B_r, \\ \text{for odd } n \geq 2 \\ 0, \text{for even } n \geq 2 \end{cases} \tag{6}$$

where the terms are defined as

$$\begin{aligned} \Lambda(\omega) &= \omega^2 I + A_r^2 \\ \Delta(\omega) &= I + e^{\frac{\pi}{\omega} A_r} \\ \Delta_r(\omega) &= I + A_\rho e^{\frac{\pi}{\omega} A_r} \\ \Gamma_r(\omega) &= \Delta_r^{-1}(\omega)\, A_\rho \Delta(\omega)\, \Lambda^{-1}(\omega) \\ \Theta_D(\omega) &= -\frac{2\omega^2}{\pi} \Delta(\omega) \left[\Gamma_r(\omega) - \Lambda^{-1}(\omega)\right]. \end{aligned} \tag{7}$$

Using Theorem 1 and the expression in (5), the open-loop frequency response of the RCS can be determined. However, due to the presence of a nonlinear element in the loop, closed-loop frequency-domain functions, such as sensitivity and complementary sensitivity, do not adhere to the conventional open-loop/closed-loop relationships observed in LTI systems. Consequently, a direct calculation of the closed-loop HOSIDFs is necessary for RCSs.

C. Closed-Loop Frequency-Domain Analysis of RCSs

As mentioned earlier, unlike LTI systems, there is no direct link between the open- and closed-loop frequency-domain response for nonlinear controllers, especially in the case of the RCS. Therefore, predicting the closed-loop performance is desirable using only frequency-domain information of the loop components, including the plant. In Theorem 2, a frequency-domain-based performance prediction for RCSs is presented under the following assumptions [11].

Assumption 1 [11, Assumption 1]: The RCS in Fig. 1 is input to state convergent.

This assumption ensures a unique periodic solution exists for the output of the reset element, which shares the same period as the reset input. Consequently, the reset output signal can be represented using a Fourier series. The validity of this assumption can be evaluated using the FRF-based method presented in [19, Corollary 1 and Th. 2]. It should be noted that the convergence and stability of all controllers in this study were verified using the aforementioned method. In addition, all designed controllers exhibited stable responses in the conducted experiments (see Section VI), which provides supporting evidence of their practical stability under the tested conditions.

Assumption 2 [11, Assumption 3]: Only the first harmonic of e_r results in resets and hence the creation of higher order harmonics ($n > 1$) in u_r.

Assumption 2 is essential for predicting the performance of closed-loop RCSs, since the method in [11] does not account for the influence of higher order harmonics on reset events. Nevertheless, [11] shows that this assumption holds when a properly designed reset controller avoids excessively large open-loop HOSIDFs, as such values can easily cause multiple zero crossings within a single cycle. In this respect, we verify, in the design of every reset controller in this study, that all controllers yield exactly two zero crossings per cycle across all frequency regions.

Theorem 2 [9, Th. 2]: Considering $r(t) = \sin(\omega t)$ and that Assumptions 1 and 2 hold, the closed-loop steady-state error $e_{ss}(t) = \lim_{t\to\infty} e(t)$ can be written as

$$e_{ss}(t) = \sum_{n=1}^{\infty} e_n(t) \tag{8}$$

where

$$e_n(t) = |S_n(j\omega)| \sin(n\omega t + \angle S_n(j\omega)) \tag{9}$$

with higher order sinusoidal-input sensitivity function $S_n(j\omega)$ as

$$S_n(j\omega) = \begin{cases} \dfrac{1}{1 + \mathcal{L}_1(j\omega)}, \text{for } n = 1 \\ -\mathcal{L}_n(j\omega)\, S_{bl}(jn\omega) \left(|S_1(j\omega)|\, e^{jn\angle S_1(j\omega)}\right), \\ \text{for odd } n \geq 2 \\ 0, \text{for even } n \geq 2 \end{cases} \tag{10}$$

where $S_{bl}(jn\omega) = 1/(1 + L_{bl}(jn\omega))$, which $L_{bl}(j\omega) = C_1(j\omega)R(j\omega)C_2(j\omega)G(j\omega)$ is the base linear transfer function of the open loop.

Theorem 2 and the results from [11] demonstrate the existence of closed-loop HOSIDFs, which must be considered for

a more precise design of reset controllers. However, analyzing reset controllers by accounting for all harmonics is a nontrivial task. To facilitate the analysis of RCSs, in [12], a method that combines all harmonics into a single frequency function is introduced. This closed-loop approximation, referred to as the pseudo-sensitivity, is defined in [12, Definition 5] as follows:

$$|S_\infty(\omega)| = \frac{\max_{0\le t<2\pi/\omega} e_{ss}(\omega, t)}{r_o} \tag{11}$$

where $e_{ss}(\omega, t)$ can be calculated from (8) based on HOSIDFs of the closed-loop system excited by $r(t) = r_0 \sin(\omega t)$ with $r_0 \in \mathbb{R}_{>0}$. The magnitude $|S_\infty(\omega)|$ over the range of frequencies of interest can approximate the sensitivity function of an RCS. While it represents the worst case scenario, it still facilitates the evaluation of various design effects. Moreover, if $|S_\infty(\omega)|$ demonstrates sufficient robustness margins, it serves as a reliable indicator of the system's performance, as it accounts for the maximum steady-state error, $\max e_{ss}(\omega, t)$.

Again, note that a parametric model of the plant is not required to calculate this pseudo-sensitivity, as Theorem 2 only necessitates the FRF of the plant. This allows for the approximation of the steady-state error based solely on the frequency response of the loop components. Utilizing the tools introduced in this section for designing and analyzing RCSs in the frequency domain, Sections III–V will illustrate their applications in the development and evaluation of an RCS for an industrial motion platform.

III. Reset-Based Filter Design: A Phase Generator Approach

Considering the CI, characterized by $A_r = 0$, $A_\rho = 0$, and $D_r = 0$ in (1), it represents the simplest form of a reset element. Unlike a linear integrator, which introduces a phase lag of $-90°$, the CI exhibits a phase lag of approximately $-38°$ in its DF (H_1 in Theorem 1) [8]. Although this advantage is evident only in the DF of reset elements, it can also be utilized to overcome the limitations of LTI controllers [20].

Building on the mentioned phase advantage, a reset-based filter is introduced in [18] to extend the application of reset control for broadband phase compensation across the desired frequency range. This so-called CgLp filter could replace part of the differentiation action in PID controllers or be used to compensate for the phase lag of any additional filter, as it helps improve the system's precision according to the loop-shaping concept [18], [21]. However, the CgLp element presented in [18] does not maintain a constant gain across all frequencies. This limitation arises from including a GFORE element combined with a lead-lag filter, which results in a gain slope of -20 dB/dec at high frequencies. This -20-dB/dec behavior originates from the nonlinear integrator component of the GFORE element, propagating the nonlinearity to very high frequencies where nonlinear action is unnecessary. In this study, we propose a proportional GFORE-based CgLp filter, where the feedthrough term in the GFORE element is nonzero ($D_r \neq 0$), achieving an almost constant gain across all frequencies.

Definition 1: In this study, we define the CgLp filter as illustrated in Fig. 2, where

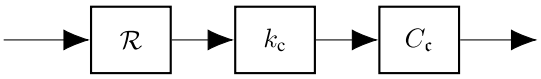

Fig. 2. CgLp filter structure.

$$k_c = \frac{\omega_f - \omega_l}{\omega_f} \tag{12}$$

$$C_c(s) = \frac{1 + s/\omega_l}{1 + s/\omega_f} \tag{13}$$

with $[\omega_l, \omega_f] \in \mathbb{R}_{>0}^{1\times 2}$, and $\mathcal{R}$ is a proportional GFORE element ($n_r = 1$) characterized by

$$A_r = -\omega_r, \quad B_r = 1, \quad C_r = \omega_r, \quad D_r = \frac{\omega_l}{\omega_f - \omega_l} \tag{14}$$

with $\omega_r \in \mathbb{R}_{>0}$ as

$$\omega_r = \frac{\omega_l}{\sqrt{1 + \left(\frac{4(1-A_\rho)}{\pi(1+A_\rho)}\right)^2}}. \tag{15}$$

The CgLp filter in Definition 1 exhibits an almost constant gain across all frequencies in its first-order DF ($\mathfrak{C}_1(\omega)$), where

$$\mathfrak{C}_n(\omega) = k_c C_c(nj\omega) H_n(\omega). \tag{16}$$

In Appendix A, we prove this characteristic of the CgLp element by demonstrating that $|\mathfrak{C}_1(\omega)| = 1$ at both low ($\omega \to 0$) and high ($\omega \to \infty$) frequencies. Since $H_1(\omega)$ represents the DF of the proportional GFORE element and cannot precisely match the magnitude of its linear counterpart, achieving an exact match across all frequencies is impossible. Consequently, a slight deviation occurs in the mid-frequency range; however, it is negligible with respect to the produced phase, similar to the findings in [18].

Furthermore, it has been demonstrated that reset elements exhibit less phase lag compared to their corresponding BLSs [8]. Consequently, the reset element $\mathcal{R}$ in the CgLp filter does not entirely cancel the positive phase contribution of the lead filter C_c within the frequency range $[\omega_l, \omega_f]$. As a result, the CgLp filter, as defined in Definition 1, introduces a positive phase within this frequency range while maintaining an approximately 0-dB gain across the entire frequency spectrum, as proven in Appendix A.

Following Definition 1, we construct the CgLp filter such that it introduces no change in gain when incorporated into a pre-designed linear controller. Additionally, it increases the phase at the frequencies of interest, thereby enabling modifications to the linear controller that were previously unattainable due to Bode's gain–phase relationship. The primary distinction between this CgLp and the one presented in [18] lies in the inclusion of a nonzero feedthrough term, D_r. This term suppresses the integral action in the GFORE element beyond a threshold frequency (ω_f), resulting in a greater difference between the magnitudes of the first-order ($\mathfrak{C}_1(\omega)$) and higher order harmonics ($\mathfrak{C}_n(\omega)$) of the CgLp element.

Thus, the use of this proportional GFORE element requires a tuning method for D_r, as, in the previous implementation of the CgLp with a GFORE element, D_r was set to zero. From

Definition 1, it can be observed that D_r can be calculated based on ω_l and ω_f. The parameter ω_l is set according to the desired corner frequency of the lead element ($C_c(j\omega)$), as it is also related to the corner frequency of the DF of the GFORE, ω_r, as well. Depending on the system dynamics and external disturbances, ω_l can be tuned accordingly. In [18], ω_f appears only in C_c and is typically set sufficiently large ($\omega_f \gg \omega_l$). However, in this context, since ω_f directly influences D_r, we aim to determine its value based on known parameters and the desired phase produced by the CgLp element (θ_{CgLp}). This method obviates the need for introducing an additional parameter for tuning. In the following lemma, we show that the maximum achievable phase of the CgLp occurs as $\omega_f \to \infty$. Then, we introduce a theorem in which ω_f is calculated based on any required phase of the CgLp filter within the achievable range.

Lemma 1: Let $\theta_M(\omega)$ denote the maximum achievable phase of the CgLp at the frequency $\omega \in \mathbb{R}_{>0}$, defined as

$$\theta_M(\omega) = \max_{\omega_f \in [\omega_l, \infty)} \left(\theta_{\mathrm{CgLp}}(\omega, \omega_f)\right) \tag{17}$$

where ω_l and A_ρ are fixed. Then, $\theta_{\mathrm{CgLp}}(\omega, \omega_f) = \theta_M(\omega)$ if and only if $\omega_f \to \infty$.

Proof: Having $\mathfrak{C}_1(\omega)$ as the DF of the CgLp element as follows:

$$\mathfrak{C}_1(\omega) = k_c H_1(\omega) C_c(j\omega) \tag{18}$$

for $\theta_{\mathrm{CgLp}}(\omega, \omega_f)$, we have

$$\theta_{\mathrm{CgLp}}(\omega, \omega_f) = \arctan\left(\frac{b(\omega)}{a(\omega) + \frac{\omega_l}{\omega_f - \omega_l}}\right) + \arctan\left(\frac{\omega}{\omega_l}\right) - \arctan\left(\frac{\omega}{\omega_f}\right) \tag{19}$$

with (based on Theorem 1)

$$\begin{aligned} a(\omega) &= \Re\left(C_r(j\omega I - A_r)^{-1}(I + j\Theta_D(\omega))B_r\right) \\ b(\omega) &= I\left(C_r(j\omega I - A_r)^{-1}(I + j\Theta_D(\omega))B_r\right) \end{aligned} \tag{20}$$

where $\Re(\cdot)$ denotes the real part and $I(\cdot)$ denotes the imaginary part. For simplicity, in the remainder of this article, we use a and b instead of $a(\omega)$ and $b(\omega)$, respectively. Moreover, it can be observed that $a(\omega)$ and $b(\omega)$ are independent of ω_f.

Since arctan is a monotonically increasing function, the expressions $\max(b(\omega)/(a(\omega) + \omega_l/(\omega_f - \omega_l)))$ and $\min(\omega/\omega_f)$ result in the maximum value of $\theta_{\mathrm{CgLp}}(\omega, \omega_f)$ in (19), where by having $\omega_f \to \infty$, resulting in

$$\frac{\omega}{\omega_f} \to 0$$

and

$$\left(\frac{b(\omega)}{a(\omega) + \frac{\omega_l}{\omega_f - \omega_l}}\right) \to \frac{b(\omega)}{a(\omega)}.$$

Thus, for fixed values of $a(\omega)$ and $b(\omega)$, $\theta_{\mathrm{CgLp}}(\omega, \omega_f) = \theta_M(\omega)$ if and only if $\omega_f \to \infty$.□

Based on the maximum achievable phase of the CgLp element, as derived in Lemma 1, the following theorem calculates the required value of ω_f (and consequently D_r) to achieve the desired phase of the CgLp, $\theta_{\mathrm{CgLp}} \in (0, \theta_M)$.

Theorem 3: Given that $\theta_{\mathrm{CgLp}}(\omega) \in (0, \theta_M(\omega))$ represents the desired phase of the DF of the CgLp filter ($\mathfrak{C}_1$), the frequency $\omega_f \in [\omega_l, \infty)$ can be determined as follows (for known ω_l and A_ρ):

$$\omega_f = \begin{cases} \min\left(\omega_{f_1}, \omega_{f_2}\right), & \text{if both } \omega_{f_1}, \omega_{f_2} \in [\omega_l, \infty) \\ \max\left(\omega_{f_1}, \omega_{f_2}\right), & \text{otherwise} \end{cases} \tag{21}$$

where

$$\begin{aligned} \omega_{f_1} &= \frac{-k_2 - \sqrt{k_2^2 - 4k_1k_3}}{2k_1} \\ \omega_{f_2} &= \frac{-k_2 + \sqrt{k_2^2 - 4k_1k_3}}{2k_1} \\ k_1 &= aQ(\omega) - b \\ k_2 &= b\omega Q(\omega) + b\omega_l + a\omega - (a-1)\omega_l Q(\omega) \\ k_3 &= -\omega\omega_l(bQ(\omega) + a - 1) \end{aligned} \tag{22}$$

with

$$Q(\omega) = \tan\left(\theta_{\mathrm{CgLp}}(\omega) - \arctan\left(\frac{\omega}{\omega_l}\right)\right). \tag{23}$$

Proof: See Appendix B.

As stated in Lemma 1, the maximum phase of the CgLp filter can be achieved by allowing $\omega_f \to \infty$. However, this implies that the nonlinear integrator component of the CgLp must remain active at very high frequencies, which increases the influence of higher order harmonics in the system. To address this, Theorem 3 provides the necessary calculation for ω_f to achieve the desired $\theta_{\mathrm{CgLp}}(\omega)$ at a specific frequency. This approach enables the designer to mitigate the impact of higher order harmonics without introducing an additional degree of tuning, which might be undesirable.

In Fig. 3(a), the first- and third-order DFs of the CgLp element are depicted for both the conventional and modified CgLp configurations. Both versions share the same parameters; however, in the conventional CgLp, the feed-through term (D_r) is set to zero, as in [18].

It can be observed that the first-order harmonic in the modified CgLp filter is positioned further away from its third-order harmonic, thereby enhancing reliability in DF-based loop-shaping control design. This effect is further illustrated in Fig. 3(b), where the relative magnitude of the third-order DF over the first-order DF ($|\mathfrak{C}_3(\omega)|/|\mathfrak{C}_1(\omega)|$) is plotted in percentage for both CgLp cases, clearly demonstrating how the feedthrough term contributes to the reliability of the DF analysis. Additionally, it can be seen that at high frequencies, in the presence of the feedthrough term, this ratio approaches zero, minimizing the impact of higher order harmonics on system performance.

Furthermore, it is evident that in this new CgLp filter, the gain remains almost constant not only up to a threshold frequency but also extends to $\omega \to \infty$. This property ensures that by incorporating this filter into a pre-designed linear controller, the system's loop gain remains consistent while simultaneously improving phase characteristics. This advantage is particularly beneficial in scenarios where a linear controller has already been implemented. In such cases, an

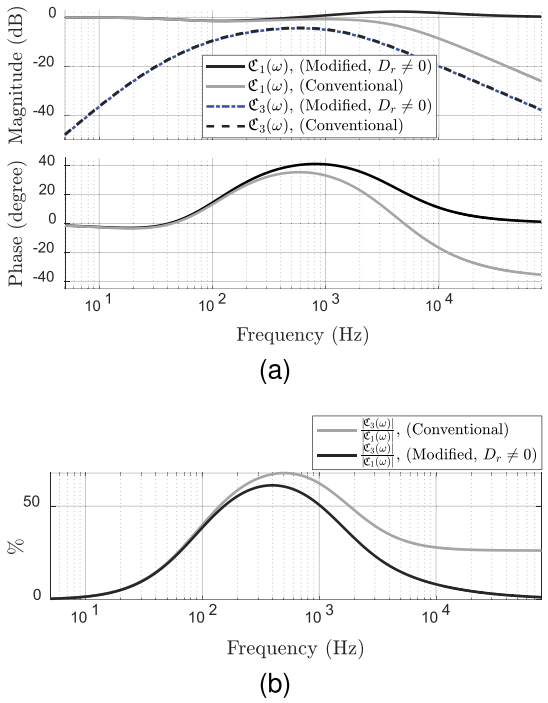

Fig. 3. (a) First- and third-order DFs of the CgLp element in both modified and conventional cases with $\omega_l = 6.28 \times 10^2$ rad/s, $\omega_f = 2.51 \times 10^4$ rad/s, and $A_\rho = 0$ (D_r is set to zero for the conventional case). (b) Relative magnitude between the third- and first-order harmonics of the CgLp elements.

add-on filter can be employed, allowing the nonlinear filter to be directly applied without altering the existing linear controller. This approach enhances system performance further while maintaining the integrity of the original control design.

In Section IV, we introduce an industrial motion stage where the limitations of the linear controllers leave no room for further improvement. Subsequently, in Section V, we demonstrate how the proposed new CgLp filter effectively addresses the existing control challenges in this industrial setup.

IV. Industrial Case Study

This section provides a detailed overview of an industrial wire-bonding machine, outlines the control objectives, introduces the optimal linear controller designed specifically for the system, and discusses the challenges that remain after implementing linear control.

A. Wire-Bonding Process

A wire bonder [see Fig. 4(a)] is a machine that connects conducting wires between an integrated circuit and its packaging, forming a microchip. It bonds the wire's ends to their underlying surfaces using thermal or ultrasonic energy.

The motion platform of the wire bonder possesses three degrees of freedom, which are controlled using a Cartesian coordinate system. To facilitate understanding, a simplified Simscape multibody model of the wire bonder's motion platform is provided in Fig. 4(b). This figure also illustrates the base frame, whose primary function is to isolate vibrations between the motion stages and the external environment. Each

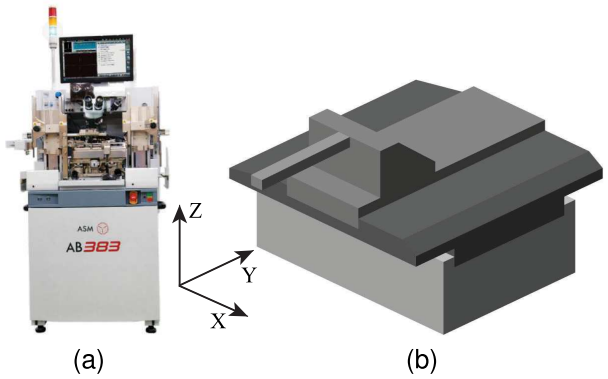

Fig. 4. (a) Industrial wire bonder. (b) Simscape multibody model of the wire bonder motion platform.

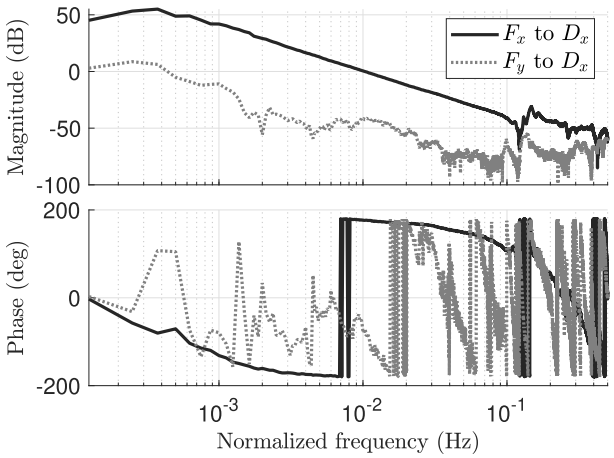

Fig. 5. FRF of the X-stage of the physical wire bonder, illustrating the mapping of actuator forces in the X-stage (F_x) and Y-stage (F_y) to the displacement measured by the X-stage encoder (D_x).

axis is equipped with a dedicated actuator that directly applies force to the respective stage. The motion stage is designed and calibrated such that each motion axis can be considered an SISO LTI system within its operational range.

Fig. 5 illustrates the measured FRF of the physical wire bonder, mapping the generated force F_x, applied to the X-stage, to the resulting displacement D_x. The FRF represents the linearized system, measured around the configuration where all three actuators are positioned at their central locations. Additionally, the figure depicts the FRF from the actuator of the Y-stage to the encoder position of the X-stage. The results indicate that cross-coupling effects are negligible up to frequencies well beyond the target control bandwidth, as the F_y to D_x response is more than 40 dB lower than the direct F_x to D_x response, corresponding to an effect of less than 1 %. The influence of actuator forces in the Z-stage on the displacement measured by the X-stage encoder is omitted from the plots, as it is even lower compared to the effect of F_y. This is expected since the Z-stage is lighter than the combined $Y{+}Z$ stage, given that the actuator in the Y-stage must drive the entire $Y{+}Z$ assembly. Consequently, the actuator in the Z-stage is less capable of exciting motion along the X-axis compared to the actuator in the Y-stage. Please note that the frequency axis

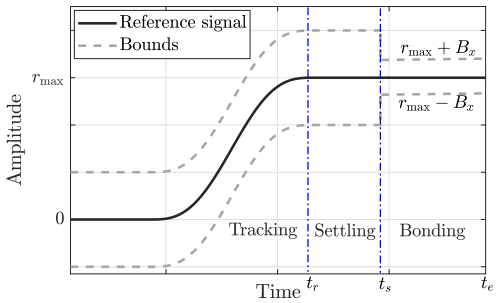

Fig. 6. Typical reference signal profile in the X-direction, divided into the tracking, settling, and bonding phases. The indicated bounds are exaggerated.

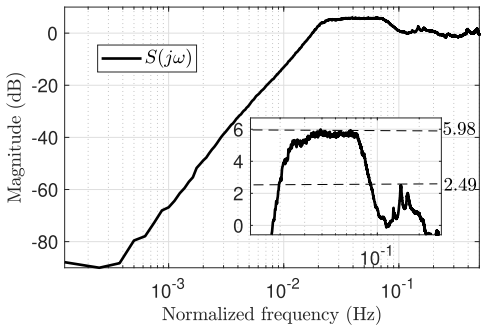

Fig. 7. Sensitivity of the wire bonder with the auto-tuned linear controller.

in Fig. 5, as well as in all other experimental results presented in this study, has been normalized for confidentiality purposes (scaled by an arbitrary factor).

Fig. 6 illustrates the general shape of the reference signal used for movement in the X-direction. The movement is divided into three distinct stages. The first stage is the tracking phase, in which the end-effector moves from one bonding surface to the next. The second stage is the settling phase, providing time for the end-effector's oscillations to stabilize within acceptable limits. The final stage, known as the bonding phase, marks the completion of the movement. Surrounding the reference signal are permissible error bounds for the end-effector. These bounds are crucial for preventing contact with previously bonded wires and surrounding objects during the tracking and settling phases. Furthermore, the error bounds during the bonding phase are necessary to ensure the end-effector remains within the bond pads. Consequently, we define the settling time of the system as the last time the position of the end-effector is located outside the $r_{\max} \pm B_x$. To give an indication of the machine precision, note that this process enables bonding with an accuracy in the micrometer range. Moreover, it operates at a rate of approximately ten wire bonds per second, highlighting its efficiency.

Therefore, a well-designed controller is required to accurately follow the reference signal with minimal error within defined boundaries. The objective is to minimize the settling region while satisfying specified frequency-domain robustness constraints. In Section IV, we present the frequency-domain constraints and evaluate the performance of an LTI controller applied to the X-stage of the wire bonder.

B. Linear Control of the Wire Bonder

Industrial motion stages are typically controlled using advanced feedforward controllers designed to follow predefined reference trajectories. Feedback control is primarily employed to enhance tracking accuracy by mitigating disturbances and addressing dynamics not accounted for by the feedforward controller. To achieve high motion control performance, a feedforward control is designed for the industrial wire bonder as well. However, the focus of this study is solely on feedback control, and the detailed information about the existing feedforward controller is intentionally omitted.

For a feedback control system with the X-stage wire bonder as the plant (G), an acceptable LTI controller (C_L) in the frequency domain must satisfy the following constraints:

$$\begin{aligned} M_s &\leq 6\,\text{dB} \\ M_r &\leq 2.5\,\text{dB} \end{aligned} \tag{24}$$

where $M_s = \max_{\omega<\omega_{\text{res}}} |S(j\omega)|$, with $S(j\omega) = 1/(1 + C_L(j\omega)G(j\omega))$ being the sensitivity function. Additionally, $M_r = \max_{\omega\geq\omega_{\text{res}}} |S(j\omega)|$, where $\omega_{\text{res}} \in \mathbb{R}_{>0}$ denotes the frequency prior to the first resonance or anti-resonance of the plant. The constraint on M_r ensures that even in the presence of inaccuracies in the measured FRF of the plant, the resonance of the system does not become excessively amplified beyond a specified robust bound. Additionally, the upper bound on the maximum magnitude of the sensitivity function (M_s) determines the robustness of the system, as the modulus margin (MM) follows the equality $\text{MM} = 1/M_s$, where MM denotes the shortest distance between the Nyquist curve of the open-loop FRF and the point $(-1, 0j)$ in the Nyquist diagram. In this study, an automatically tuned LTI controller is considered to push performance to the limits of linear control. The controller aims to achieve optimal tracking performance, maximizing the bandwidth while increasing the loop gain, and simultaneously satisfying the robustness conditions outlined in (24).

Having the $C_L(j\omega)$ as the automatically tuned discretized linear controller and G as the FRF of the industrial wire bonder, the sensitivity function is plotted in Fig. 7. It can be observed that the auto-tuner algorithm designed an LTI controller to reduce the magnitude of the sensitivity at low frequencies while maintaining certain robust bounds. The broad range of the sensitivity peak enables a reduction in its magnitude at low frequencies due to the waterbed effect.

The designed LTI controller is implemented on the X-stage of the industrial wire bonder motion platform. Fig. 8(a) presents the error profile of the end-effector's position as it attempts to follow a trajectory $r_1(t)$, which resembles the typical trajectory depicted in Fig. 6, with $\max_{\forall t\in\mathbb{R}_{\geq 0}} |r_1(t)| = r_{1,\max}$. We define the stationary region as $[t_r, t_e]$ (see Fig. 6), where t_r represents the first time the reference signal reaches $r_{\max}$ (or 0 for backward motion), and t_e denotes the last time it remains at that value (the moment just before beginning the next motion).

In Fig. 8(b), the power spectral density (PSD) of the error is depicted, focusing on the samples within the stationary region $[t_r, t_e]$ after the forward motion is finished. The analysis reveals that the majority of the error energy is concentrated around

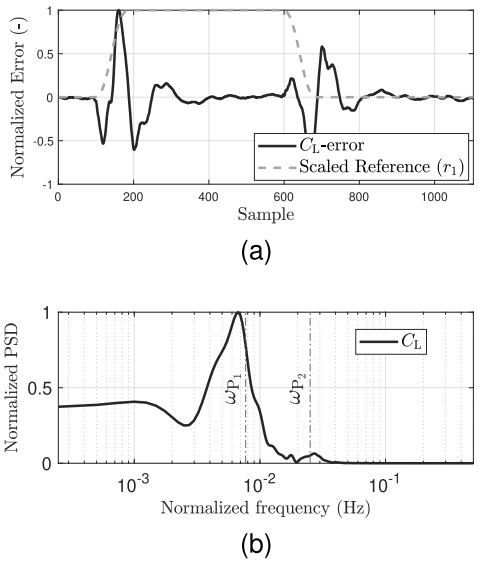

Fig. 8. (a) Normalized error signal for both forward and backward motion under linear control. (b) Normalized PSD of the error within the stationary region.

ω_{P_1}, primarily corresponding to the frequency of the base-frame vibration. This phenomenon arises from the reaction force exerted by the actuator on the base frame, which is subsequently transmitted to the end-effector. This low-frequency vibration persists as a disturbance within the low-frequency range, remaining in the system even after the motion has concluded ($t \in [t_r, t_e]$). Notably, the peak of the PSD in Fig. 8(b) does not exactly coincide with ω_{P_1}, as some error from the transient response remains and influences the location of the base-frame vibration. By computing the PSD slightly after t_r, these values would align more closely. However, in this study, we take the PSD from the moment the motion is first finished (t_r) for the sake of consistency throughout the analysis.

To suppress this base-frame vibration, the magnitude of the sensitivity function at low frequencies must be reduced. However, due to the limitations of linear control—specifically, the waterbed effect—either the robust bounds would be violated, or the magnitude of the sensitivity at other frequencies would be amplified. Additionally, the analysis indicates an error arising from frequencies (ω_{P_2}) around the sensitivity peak (near the bandwidth), which is the region where the most energy transitions from the reference signal to the error ('$S = e/r$'). Consequently, this frequency range should also be considered as a potential source of excitation by different input references.

Given these constraints and the inherent limitations of linear control in further improving the performance of this motion platform, Section V presents the design and implementation of a reset-based filter. This filter, informed by the results from Section III, aims to outperform the currently implemented linear controller.

V. Reset Control Design for the Wire Bonder

In this section, building upon the CgLp filter introduced in Section III, we aim to design a filter that can be integrated with the existing linear controller C_L. This filter is intended to reduce the magnitude of the sensitivity function around the frequencies of interest while ensuring that the magnitude of the function at other frequencies, particularly the robust bounds, remains unaffected.

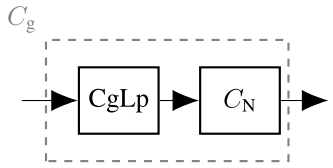

Fig. 9. Add-on filter (C_g) structure.

In this study, we aim to incorporate an add-on nonlinear-based filter because it does not require any modifications to the existing linear control system. Moreover, the linear controller does not need to adapt to the designed nonlinear controller. This characteristic is particularly appealing for industrial applications where an LTI controller is already implemented, and the objective is to enhance its performance without compromising its existing functionality. In this context, we introduce the following performance improvement criterion, which provides a direct measure of the extent to which adding nonlinearity enhances system performance. Accordingly, we define the sensitivity improvement indicator (δ_s) as

$$\delta_s(\omega) = \frac{|S_\infty(\omega)| - |S(j\omega)|}{|S(j\omega)|}\% \tag{25}$$

where $S(j\omega)$ is the sensitivity of the linear control system and $S_\infty(\omega)$ is the (pseudo-) sensitivity [see (11)] of the RCS in which a nonlinear controller has been added to the existing linear control system.

A. Frequency-Domain Filter Design

To reduce the magnitude of the sensitivity function around the base-frame vibration frequencies (ω_{P_1}), we propose incorporating an inverse notch filter into the controller C_L. However, the inverse notch filter introduces negative phase shifts at frequencies beyond its effective range, which can reduce the phase margin and amplify the sensitivity function's peak magnitude. Both effects may lead to a violation of the constraints specified in (24).

To address this issue, we combine the inverse notch filter with the CgLp filter presented in Definition 1. This combination compensates for the phase loss introduced by the inverse notch filter, thereby maintaining the phase margin and preserving the magnitude characteristics around the sensitivity peak. Thus, we design this add-on filter (C_g) as illustrated in Fig. 9. The C_N represents the inverse notch filter, described as

$$C_N(s) = \frac{s^2/\omega_n^2 + s/(\omega_n Q_1) + 1}{s^2/\omega_n^2 + s/(\omega_n Q_2) + 1} \tag{26}$$

where the peak of the inverse notch occurs at $\omega_n \in \mathbb{R}_{>0}$ with a magnitude of $Q_2/Q_1 > 1$ ($Q_1, Q_2 \in \mathbb{R}_{>0}$).

To specifically target the peak of the error energy at ω_{P_1}, we adopt the following procedure for designing the add-on filter C_g.

1) Select $\omega_n = \omega_{P_1}$ with appropriate values for Q_1 and Q_2 to achieve sufficient width and height in the inverse notch filter's magnitude (Q_1 and Q_2 should be chosen based on the magnitude and width of the PSD at the problematic frequency).
2) Determine the required phase of the CgLp filter as the phase lost due to the inverse notch filter at the bandwidth frequency (the open-loop crossover frequency, ω_c) of the existing linear controller C_L

$$\theta_{\text{CgLp}}(\omega_c) = -\angle C_N(\omega_c). \tag{27}$$

3) Choose ω_l within the interval $[\omega_{P_1}, \omega_c]$. This selection ensures that nonlinearity is not concentrated near the problematic frequency (ω_{P_1}) while still providing sufficient phase at the bandwidth frequency.
4) Select the desired value of A_ρ. (In this study, we consider $A_\rho = 0$ for all reset elements.) Use the required θ_{CgLp}, along with the selected ω_l and A_ρ, to calculate the required ω_f (using Theorem 3).
5) Shape the CgLp components (k_c, $\mathcal{R}$, and $C_\mathfrak{c}$) based on the calculated ω_f (using Definition 1).
6) Design the add-on filter as Fig. 9, based on the designed CgLp and C_N filter.
7) Design the closed-loop control system as shown in Fig. 1, with $C_1 = 1$, $C_2 = k_c \cdot C_\mathfrak{c} \cdot C_N \cdot C_L$.
8) Compute the pseudo-sensitivity, $S_\infty(\omega)$, for the designed reset-based controller and verify its compliance with the constraints presented in (24).
9) If both constraints in (24) are satisfied and a sufficient reduction in $|S_\infty(\omega)|$ at the problematic frequency is achieved, then the designed nonlinear controller is considered valid. However, if one or both constraints are violated, the frequency ω_l may need to be reselected or a less aggressive gain filter—specifically, the inverse notch filter (C_N)—may (C_N)—may be used instead. This adjustment is necessary because a less aggressive inverse smaller negative phase shift at the bandwidth frequency, thereby reducing the nonlinear action required from the CgLp element. As a result, the higher order harmonics and $|S_\infty(\omega)|$ around the bandwidth are mitigated, increasing the likelihood of satisfying the constraints and ensuring the validity of the controller.

Please note that the above steps can be applied to any other filter in place of C_N by simply selecting a different filter in (26). Additionally, regarding Assumption 2, and to obtain a more reliable approximation of the predicted closed-loop performance, we verify that the designed reset-based controller results in exactly two zero crossings per period for the signal e_r across the frequency range. Satisfying this additional condition does not necessarily confirm that Assumption 2 holds; however, it helps eliminate an obvious case of violation in this assumption and enhances the reliability of the results.

Considering the vibration frequency of the base frame depicted in Fig. 8(b) as the target frequency, we select the parameters for C_N as $\omega_n = 48.38 \times 10^{-3}$ rad/s ($\omega_n = \omega_{P_1}$), $Q_1 = 1.31$, and $Q_2 = 1.62$. Having the bandwidth of the linear controller (C_L) at 18.4×10^{-2} rad/s, we take the aforementioned reset controller design steps, we select $A_\rho = 0$, and $\omega_l = 11.75 \times 10^{-2}$ rad/s and calculate the rest of the parameters based on Definition 1 and Theorem 3 and consequently the add-on filter.

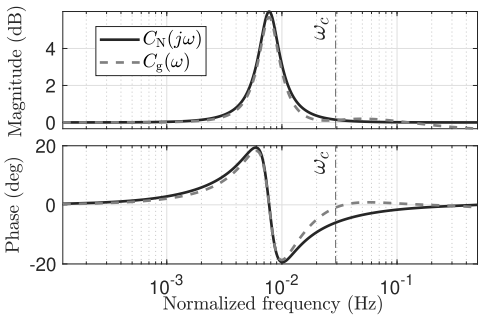

Fig. 10. Added gain to the system, with (C_g) and without (C_N) the CgLp part.

It is also essential to highlight that, in this study, we are employing an optimal linear controller that is already operating at its limits, as can be observed in Fig. 7. Consequently, it becomes challenging to avoid violating the second constraint in (24) after implementing the reset-based filter. To address this, we adopt a strategy that ensures compliance with the high-frequency constraint.

Specifically, in scenarios where the first constraint ($M_s \leq 6$ dB) is satisfied, and a sufficient reduction is achieved around the desired frequency, but a minor violation occurs in M_r, we set the frequency of the lead element ($C_\mathfrak{c}$) as ω_f/c_f, where $c_f \geq 1$ is chosen to be close to one (e.g., $c_f \in [1, 1.1]$). This results in a slight reduction in $|S_\infty(\omega)|$ around the resonance frequency (ω_{res}), thereby ensuring compliance with the constraint on M_r.

It should be noted that this approach is effective only if the violation in M_r is not significant. Otherwise, larger values of c_f would be required, which could, in turn, impact M_s.

Fig. 10 illustrates the inverse notch filter, $C_N(j\omega)$, alongside the DF of the add-on filter, $C_g(\omega)$. The DF of the add-on filter is defined as $C_g(\omega) = \mathfrak{C}_1(\omega) \cdot C_N(j\omega)$. It can be observed that the filter $C_g(\omega)$ exhibits nearly identical magnitude characteristics to $C_N(j\omega)$ without introducing a negative phase at the bandwidth frequency. The effect of the proposed strategy (incorporation of c_f) is also evident in Fig. 10, where the gain of the add-on filter slightly decreases at high frequencies (with $c_f = 1.06$).

The designed add-on filter is subsequently implemented to enhance the performance of the linear controller C_L, thereby shaping the reset-based controller C_{NL1}, with $C_1 = 1$, $C_2 = k_c \cdot C_\mathfrak{c} \cdot C_N \cdot C_L$, and $\mathcal{R}$ functions as a proportional GFORE element defined by the parameters ($\mathcal{R} : A_r = -\omega_r$, $B_r = 1$, $C_r = \omega_r$, $D_r = \omega_l/(\omega_f - \omega_l)$).

Utilizing Theorem 2 and (11), we calculate the pseudo-sensitivity for the designed C_{NL1} controller. In Fig. 11(a), the pseudo-sensitivity ($S_\infty(\omega)$) of the designed reset-based controller (C_{NL1}) is plotted alongside the sensitivity of the linear controller (C_L). It is observed that the magnitude of the sensitivity is reduced at the problematic frequency (ω_{P_1}) for the controller, while all robustness constraints are satisfied for this controller. To better observe this, the Bode sensitivity

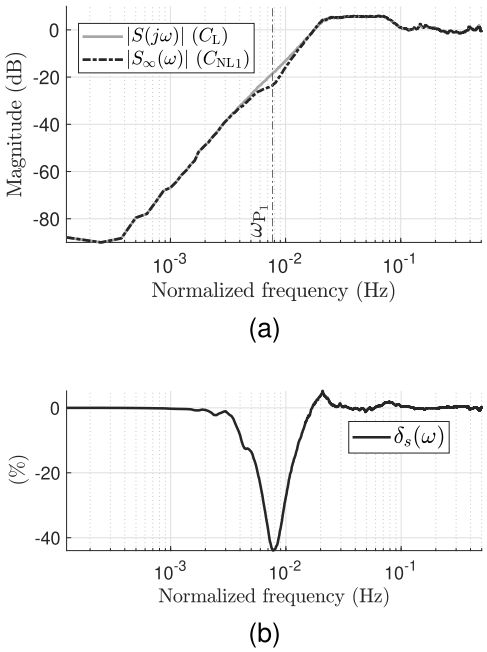

Fig. 11. (a) (Pseudo-) sensitivity magnitude for C_L and C_{NL1}. (b) Sensitivity improvement indicator for controller C_{NL1}.

integral has been calculated for both controllers as

$$\int_{f_1}^{f_{\text{end}}} \ln|S\ (j\omega)|\, d\omega = 9.83 \tag{28}$$

and

$$\int_{f_1}^{f_{\text{end}}} \ln|S_\infty(\omega)|\, d\omega = -7.46 \tag{29}$$

where $[f_1, f_{\text{end}}]$ is the frequency range where the plant is identified. The calculated Bode sensitivity integrals show that the reset-based controller (C_{NL1}) results in a reduction of 17.3 compared to the linear controller.

To better observe the effect of the added filter on the sensitivity of its linear counterpart, we utilize the sensitivity improvement indicator ($\delta_s(\omega)$) presented in (25). The $\delta_s(\omega)$ value, calculated using the sensitivities of C_L and C_{NL1}, is shown in Fig. 11(b). This metric provides a clearer understanding of the impact of incorporating the nonlinear element in the closed-loop control system.

As depicted in Fig. 11(b), negative values of $\delta_s(\omega)$ indicate a reduction in the energy of the error at corresponding frequencies, suggesting improved performance. It can be observed that, around the base-frame vibration frequency, the reset-based controller achieves approximately a 40% reduction in sensitivity magnitude compared to the linear controller. Conversely, positive values of $\delta_s(\omega)$ suggest that if those frequencies are excited, the nonlinearity introduced by the reset element could lead to higher error levels compared to the linear controller. This insight enables the designer to shape the controller more effectively by analyzing this FRF-based factor, thus avoiding error magnification around critical frequencies during the design process.

After designing and validating the reset-based controller in the frequency domain, we aim to implement it on the physical wire bonder. Before proceeding, we outline practical guidelines for the discrete-time implementation of this reset-based controller. Finally, we validate its effectiveness through time-domain experiments.

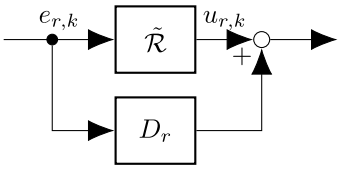

Fig. 12. Discrete-time implementation of the proportional GFORE element.

B. Practical Guidelines for the Implementation of Linear and Reset Controllers

All linear and reset controllers discussed in this study are implemented in a digital framework. The discretization of all LTI elements is performed using the Tustin approximation method, which provides adequate phase preservation of the continuous-time system compared to other approximation techniques, especially up to frequencies close to the Nyquist frequency [22]. Additionally, all frequency responses associated with linear elements are expressed in discrete time (discretized FRF).

The discrete-time realization of the reset element in (1) (for the FORE, $n_r = 1$) is presented as Fig. 12. Since D_r in (1) represents only the feedthrough term, which can be placed in parallel with the GFORE element, we provide the discrete-time realization for the case where $D_r = 0$ and subsequently add D_r to the discretized output. Thus, we obtain

$$\tilde{\mathcal{R}} := \begin{cases} x_{r,k+1} = \tilde{A}_r x_{r,k} + \tilde{B}_r e_{r,k}, & \text{if } \left(e_{r,k}, e_{r,k-1}\right) \notin \tilde{\mathcal{F}} \\ x_{r,k+1} = A_\rho \left(\tilde{A}_r x_{r,k} + \tilde{B}_r e_{r,k}\right), & \text{if } \left(e_{r,k}, e_{r,k-1}\right) \in \tilde{\mathcal{F}} \\ u_{r,k} = \tilde{C}_r x_{r,k} + \tilde{D}_r e_{r,k}, & \text{if } \left(e_{r,k}, e_{r,k-1}\right) \notin \tilde{\mathcal{F}} \\ u_{r,k} = A_\rho \left(\tilde{C}_r x_{r,k} + \tilde{D}_r e_{r,k}\right), & \text{if } \left(e_{r,k}, e_{r,k-1}\right) \in \tilde{\mathcal{F}} \end{cases} \tag{30}$$

with

$$\tilde{\mathcal{F}} := \left\{\left(e_{r,k}, e_{r,k-1}\right) \in \mathbb{R}^2 \,\middle|\, e_{r,k} = 0 \ \vee\ e_{r,k} e_{r,k-1} < 0\right\} \tag{31}$$

where $\tilde{A}_r$, $\tilde{B}_r$, $\tilde{C}_r$, and $\tilde{D}_r$ all $\in \mathbb{R}$ represent the state-space matrices of the Tustin-discretized BLS (GFORE with A_r, B_r, C_r, and $D_r = 0$), and $k \in \mathbb{N}$ denotes the sample index. The system primarily follows the Tustin-discretized linear dynamics. However, if a reset is detected, the state and the output are reset to A_ρ times their original values.

It should be noted that in this study, we used a different and more precise reset surface compared to other studies, such as [9]. Specifically, the system in (30) resets its state $x_{r,k+1}$ when either $e_{r,k} = 0$ or $e_{r,k} e_{r,k-1} < 0$. A limitation of the previous discrete reset surface, as defined by the condition

$$\tilde{\mathcal{F}} := \left\{\left(e_{r,k}, e_{r,k-1}\right) \in \mathbb{R}^2 \mid e_{r,k} e_{r,k-1} \le 0\right\}$$

presented in [9], was that it triggered a reset at both sample $k-1$ and k when $e_{r,k-1} = 0$. This behavior resulted in two resets occurring for a single zero crossing.

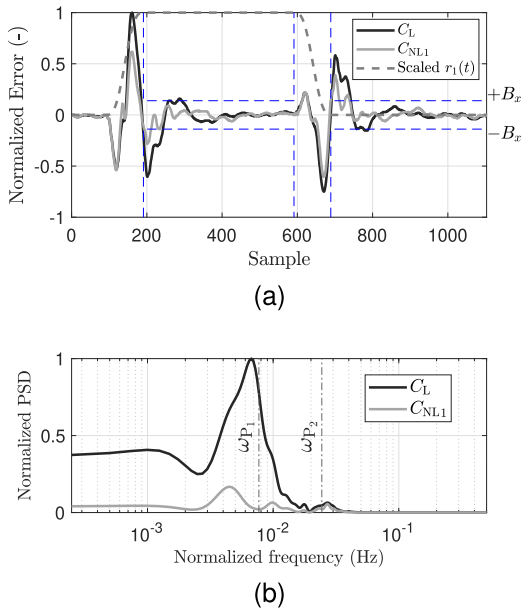

Fig. 13. (a) Normalized error signal for both forward and backward motion for linear and nonlinear controllers. (b) Normalized PSD of the error within the stationary region of forward motion.

It is important to emphasize that, although the actual zero crossing occurs between samples $k-1$ and k, approximating sample k as the reset event sample and performing discretization do not introduce significant inaccuracies in continuous-time HOSIDF analysis (the method used in this work to represent the reset element in the frequency domain). This is because, in this study, the reset element is considered as a proportional GFORE with a nonzero feedthrough term. As a result, the nonlinearity is effectively attenuated well below the sampling frequency ($\omega_f \approx F_s/30$, where F_s denotes the sampling frequency). Furthermore, since the bandwidth frequency is located approximately around ω_f, it is reasonable to assume that this approximation does not introduce significant errors, particularly in terms of DF-based phase analysis around the bandwidth frequency.

With the reset element digitally implemented, we next present the experimental results of applying reset-based controllers to the wire bonder.

VI. Experimental Results

In this section, we implement the designed reset controller, C_{NL1}, on the physical wire bonder, considering the reference trajectory $r_1(t)$. A comparison is then made with its linear counterpart controller. Fig. 13(a) presents the error profiles for both C_L and C_{NL1}. A clear reduction in the error is observed. To quantify this performance, we define $T^\star \in \mathbb{R}_{>0}$ as the time interval from the moment the motion is completed (t_r, as depicted in Fig. 6) until the error last remains outside the $\pm B_x$ bound. Evidently, the objective is to minimize this region, enabling the system to transition more quickly to the bonding phase, thereby increasing the overall bonding efficiency. Mathematically, $T^\star$ is expressed as

$$T^\star = t_s - t_r \tag{32}$$

where $t_s \in \mathbb{R}_{>0}$ represents the settling time, defined as

$$t_s = \min \left\{ t \in [t_r, t_e] \;\middle|\; |e(t)| \leq B_x \quad \forall\, t \geq t_s \right\}. \tag{33}$$

In Fig. 13(a), the $\pm B_x$ bound is scaled relative to the error. By calculating $T^\star$ for both the linear and nonlinear cases, it is demonstrated that the reset-based filter $C_{NL1}C_{NL1}$ reduces the settling duration ($T^\star$) by 80.4% for forward motion and 50.5% for compared to the linear controller C_L.

In the linear control setup, when the end-effector reached its final position, vibrations in the base frame necessitated waiting for the oscillations to dampen before the system could stabilize within the defined boundary. This delay was critical to ensure precise connections and avoid collisions with adjacent wires. By incorporating the reset-based filter into the control loop without altering any mechanical components of the machine, the system achieved significantly faster transitions to the bonding phase by effectively damping unwanted vibrations. Notably, since these forward and backward motions occur multiple times per second, the 80.4% improvement in forward motion and 50.5% improvement in backward motion significantly enhance the efficiency of the machine. Consequently, this leads to a substantial increase in the number of microchips packaged.

The PSD of the errors is also calculated for the stationary region $[t_r, t_e]$ and is depicted in Fig. 13(b). For simplicity, only the PSD corresponding to the forward motion is that it is evident that the energy of the error is significantly reduced at the base-frame vibration frequency (ω_{P_1}). This observation demonstrates how the waterbed effect has been mitigated, enabling the reduction of error at a specific frequency without compromising performance at other frequencies. To quantify this performance, the root mean square (rms) of the error is calculated for the stationary region $[t_r, t_e]$. The results indicate a 58.9% reduction in rms error for forward motion and a 46.4% reduction for backward motion. The reduction in the rms value is as important as the reduction in the settling period. While the goal of minimizing the settling period was to enable the system to reach the bonding region as quickly as possible, the reduction in rms error demonstrates that the end-effector remains in the target position with a significantly lower deviation from the desired point. This improvement contributes to higher accuracy during the bonding process. Consequently, the incorporation of the reset-based filter resulted in enhancements to both the speed and accuracy of this wire bonder machine.

Thus far, we have analyzed the control challenges associated with trajectory tracking of the reference signal $r_1(t)$. The problematic frequency (ω_{P_1}) identified may arise exclusively for this specific reference. Therefore, in Section VI-A, we present a robust reset controller capable of enhancing system performance for tracking various potential reference trajectories.

A. Robust Control Design

In Section IV-B, we illustrated and discussed the presence of base-frame vibrations in the error signal while the system attempted to follow the reference trajectory $r_1(t)$. During the wire-bonding process, the end-effector typically moves from

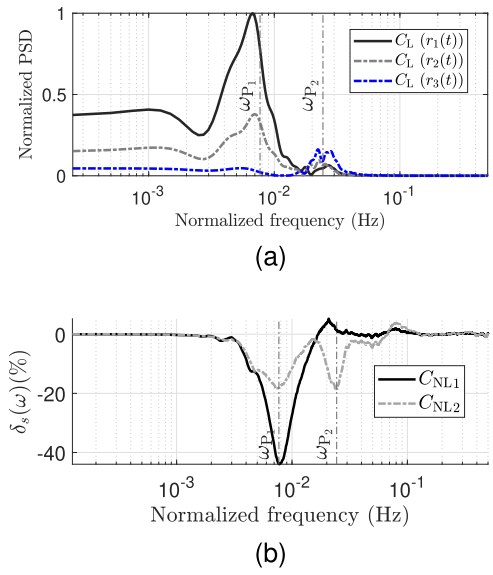

Fig. 14. (a) PSD of the error for the controller C_L following $r_1(t)$, $r_2(t)$, and $r_3(t)$. (b) Sensitivity improvement indicator for the controller C_{NL2}, designed to target multiple problematic frequencies.

one point to another. These movements can be categorized as short-range, mid-range, or long-range motions. Although $r_1(t)$ is scaled in Section IV-B for confidentiality reasons, it represents a long-range reference trajectory. The energy spectrum of these long-range motion setpoints primarily consists of low-frequency components, which excite base-frame vibrations and subsequently affect the position of the end-effector, leading to error concentration at ω_{P_1}.

However, as the motion range decreases, the energy associated with the error gradually shifts from base-frame vibrations (ω_{P_1}) to vibrations near the bandwidth frequency (ω_{P_2}). This shift occurs because the bandwidth frequency exhibits the highest energy levels, as indicated by the sensitivity analysis. Additionally, short-range input reference signals typically contain high-frequency components in their energy spectrum, which have a greater impact on error at higher frequencies during short movements. To further investigate this behavior, we study two additional reference trajectories, $r_2(t)$ and $r_3(t)$, where

$$\max_{\forall t \in \mathbb{R}_{\geq 0}} |r_2(t)| = r_{2,\max} = r_{1,\max}/2$$

and

$$\max_{\forall t \in \mathbb{R}_{\geq 0}} |r_3(t)| = r_{3,\max} = r_{1,\max}/10.$$

It should be noted that the reference trajectories $r_2(t)$ and $r_3(t)$ are not only shorter in distance but also shorter in duration compared to $r_1(t)$. The linear controller C_L is implemented for both reference trajectories $r_2(t)$ and $r_3(t)$. The PSD of the error regarding the three different reference trajectories is illustrated in Fig. 14(a). It is observed that the magnitude of the PSD for $r_2(t)$ is distributed across both ω_{P_1} and ω_{P_2} frequencies, whereas for $r_3(t)$, the magnitude of the PSD is concentrated almost entirely at ω_{P_2}. Consequently, the nonlinear controller C_{NL1} may not perform optimally for reference trajectories $r_2(t)$ and $r_3(t)$, as it is designed to reduce error around the ω_{P_1} frequency and following $r_2(t)$ and $r_3(t)$ with this controller might not result in any improvement at ω_{P_2} frequency.

TABLE I

IMPROVEMENT VALUES FOR SETTLING PERIOD AND RMS ERROR FOR C_{NL1} AND C_{NL2} COMPARED TO C_L

Reference	$C_{\mathrm{NL}1}$		$C_{\mathrm{NL}2}$	
	$T^\star$ Change (%)	RMS error Change (%)	$T^\star$ Change (%)	RMS error Change (%)
$r_1(t)$-Forward	-80.4	-58.9	-54.9	-51.4
$r_1(t)$-Backward	-50.5	-46.4	-51.5	-39.9
$r_2(t)$-Forward	+2.9	-31.6	-25.7	-32.6
$r_2(t)$-Backward	+0.7	-19.3	-28.8	-21.9
$r_3(t)$-Forward	-0.8	+5.3	-5.1	-23.7
$r_3(t)$-Backward	-0.3	-1.8	-3.4	-21.9
Average	-21.4	-25.5	-28.2	-31.9

Thus, we consider a gain filter that combines two inverse notches [each has the same transfer function as (26)], one at $\omega_{P_1} = 48.38 \times 10^{-3}$ rad/s and one at $\omega_{P_2} = 15.33 \times 10^{-2}$ rad/s. With this filter, denoted as $C_N(s) = C_{N_1}(s)C_{N_2}(s)$, and by selecting $\omega_l = 14.39 \times 10^{-2}$ rad/s, $A_\rho = 0$, $Q_1 = 1.12$, $Q_2 = 1.59$ (for C_{N_1}), $Q_1 = 1.43$, and $Q_2 = 1.59$ (for C_{N_2}), we can follow the exact steps outlined in Section V-A [(26) and onward] to design the new nonlinear controller. Based on the design steps and considering the sequence of the elements as $C_1 = C_{N_2}$ (we had to move the C_{N_2} filter before the reset element due to a firmware limitation on the maximum order of filters that can be implemented in C_2), $C_2 = k_c \cdot C_c \cdot C_{N_1} \cdot C_L$, a valid controller ($C_{NL2}$) is selected, which satisfies all constraints in (24), and results in the reduction of $|S_\infty(\omega)|$ in both ω_{P_1} and ω_{P_2}.

The sensitivity improvement indicator for the controller C_{NL2} is depicted in Fig. 14(b). It can be observed that it does not reduce the error at ω_{P_1} as effectively as the controller C_{NL1}, but it demonstrates a reduction in sensitivity at ω_{P_2}. This makes C_{NL2} a better choice when the system must follow all trajectories in a single operation, ensuring that the error can be reduced compared to the linear controller, independent of the problematic frequency that is excited.

Following the design of C_{NL2}, it is implemented on the physical wire bonder for various setpoints $r_1(t)$, $r_2(t)$, and $r_3(t)$. Table I presents the results for the two designed nonlinear controllers (C_{NL1} and C_{NL2}), highlighting their performance in terms of settling time and rms error. These metrics are compared to those of the linear controller, with the improvements expressed as percentages (minus values mean the improvement compared to the linear controller).

It can be observed that while the controller C_{NL1} significantly reduces both the settling time and the rms error for the reference trajectory $r_1(t)$, it does not outperform the linear controller C_L for other range of motions. Therefore, in scenarios involving a combination of both short and motions, or where a controller needs to perform independently of the reference trajectory while still improving system performance, the controller C_{NL2} should be selected. As shown in Table I, this controller consistently outperforms the linear controller across all reference trajectories in terms of both settling duration and rms error reduction.

It is noteworthy that these improvements were achieved solely through the frequency-domain tuning method, leveraging pseudo-sensitivity and the newly introduced sensitivity improvement factor. This approach allows designers to shape $\delta_s(\omega)$ based on the power spectrum density analysis of a pre-designed linear controller and enhance its performance without altering the controller itself. This method is particularly advantageous in industrial applications, as it enables the frequency-domain designing and shaping of a nonlinear-based filter to improve system performance, even without access to the parametric model of the system or detailed parameters of the implemented linear controller.

VII. Conclusion

In this article, we demonstrated the design of a reset-based controller and its integration into an existing control loop without modifying other constraints or compromising the system's performance criteria. This was achieved through the introduction of a proportional FORE and the formulation of the CgLp filter based on this element. By employing this FORE with a nonzero feedthrough term, the nonlinear filter benefits could be exploited while mitigating the effects of nonlinearity beyond a certain frequency. The proposed formulation and combination of the CgLp element with any required gain-based filter (e.g., CgLp + inverse notch) allow for direct integration into an existing linear controller. This feature is particularly valuable in industrial applications where redesigning the entire control loop is often impractical.

Shaping this nonlinear filter relies on a closed-loop frequency-domain method, allowing designers to tailor the controller using only the plant's FRF. The sensitivity improvement indicator was introduced to assess the impact of added nonlinearity directly in the closed-loop response.

To validate this approach, we addressed a base-frame vibration problem in an industrial wire bonder. The objective was to resolve this issue without altering the mechanical structure or the pre-implemented linear controller while ensuring all robustness constraints were met. Experimental results demonstrated that the error energy was reduced to half of that achieved with the linear controller, and the bonding process speed was increased. To further generalize and enhance the robustness of the design, another reset-based filter was shaped using the sensitivity improvement indicator. This filter effectively targeted a broader frequency range, reducing error energy from very low frequencies up to the bandwidth frequency while maintaining robustness. Ultimately, the robust reset controller improved both the rms error and the settling time across various reference trajectories.

In conclusion, this study introduces a step-by-step design method for a phase generator reset-based filter that mitigates the negative effects of nonlinearity. The resulting add-on filter can be used to shape the control loop gain constructively without altering the existing structure, making it compatible with any linear controller.

For future work, the proposed design method could be extended and formalized as an optimization problem, where the cost functions minimize the sensitivity improvement indicator at problematic frequencies.

Appendix A
CgLp Construction

To ensure that a GFORE element ($A_r = -\omega_r, B_r = 1, C_r = \omega_r$, and $D_r = 0$) exhibits the same magnitude characteristics at low frequencies ($\omega \to 0$) and high frequencies ($\omega \to \infty$) as a linear low-pass filter ($1/(1 + j\omega/\omega_l)$), similar to the approach in [23, Sec. III], the following conditions must hold:

$$|H_1(\omega)|_{\omega\to 0} = 1 \tag{34}$$

and

$$|H_1(\omega)|_{\omega\to\infty} = \frac{\omega_l}{\omega}. \tag{35}$$

From Theorem 1, the magnitude $|H_1(\omega)|$ for the given GFORE parameters can be expressed as

$$|H_1(\omega)| = \frac{\omega_r\sqrt{1+\Theta_D^2(\omega)}}{\sqrt{\omega_r^2+\omega^2}}. \tag{36}$$

Given that $\Theta_D(0) = 0$, (36) yields

$$|H_1(\omega)|_{\omega\to 0} = 1$$

which confirms that (34) holds. Furthermore, since

$$\lim_{\omega\to\infty}\Theta_D(\omega) = \frac{4\left(1-A_\rho\right)}{\pi\left(1+A_\rho\right)}$$

evaluating (36) as $\omega \to \infty$ and equating it to (35) provides the expression for ω_r

$$\omega_r = \frac{\omega_l}{\sqrt{1+\left(\frac{4\left(1-A_\rho\right)}{\pi\left(1+A_\rho\right)}\right)^2}}. \tag{37}$$

In this proof, we demonstrate that employing the CgLp configuration presented in Definition 1 leads to the following result.

1) $|\mathfrak{C}_1(\omega)|_{\omega\to 0} = 1$.
2) $|\mathfrak{C}_1(\omega)|_{\omega\to\infty} = 1$.

Thus, from (16), we have

$$|\mathfrak{C}_1(\omega)| = k_c\,|H_1(\omega)|\,|C_{\mathfrak{c}}(j\omega)|. \tag{38}$$

Using $H_1(\omega)$ from (6), this time for $A_r = -\omega_r$, $B_r = 1$, $C_r = \omega_r$, and $D_r \neq 0$, and we get

$$|H_1(\omega)| = \left|\omega_r(j\omega+\omega_r)^{-1}(1+j\Theta_D(\omega)) + D_r\right| \tag{39}$$

which results in

$$\lim_{\omega\to 0} k_c\,|H_1(\omega)|\,|C_{\mathfrak{c}}(j\omega)| = k_c(D_r+1) \tag{40}$$

and using k_c from (12) and D_r from (14), we obtain

$$|\mathfrak{C}_1(\omega)|_{\omega\to 0} = 1. \tag{41}$$

To analyze $|\mathfrak{C}_1(\omega)|_{\omega\to\infty}$, we have

$$\lim_{\omega\to\infty} k_c\,|H_1(\omega)|\,|C_{\mathfrak{c}}(j\omega)| = k_c D_r\frac{\omega_f}{\omega_l} \tag{42}$$

where by substituting k_c from (12) and D_r from (14), we obtain

$$|\mathfrak{C}_1(\omega)|_{\omega\to\infty} = 1. \tag{43}$$

From (40) and (42), it can also be observed that the values of k_c and D_r provided in Definition 1 are the only possible values that satisfy both $k_c(D_r+1) = 1$ and $k_c D_r\omega_f/\omega_l = 1$.□

APPENDIX B
PROOF OF THEOREM 3

Given the phase of the DF of the CgLp as

$$\theta_{\mathrm{CgLp}}(\omega) = \arctan\left(\frac{b}{a+\frac{\omega_l}{\omega_f-\omega_l}}\right)+\arctan\left(\frac{\omega}{\omega_l}\right)-\arctan\left(\frac{\omega}{\omega_f}\right) \quad (44)$$

we can express

$$\theta_{\mathrm{CgLp}}(\omega)-\arctan\left(\frac{\omega}{\omega_l}\right) = \arctan\left(\frac{b}{a+\frac{\omega_l}{\omega_f-\omega_l}}\right)-\arctan\left(\frac{\omega}{\omega_f}\right). \quad (45)$$

Using the identity $\arctan(x)-\arctan(y)=\arctan((x-y)/(1+xy))$, we obtain

$$\theta_{\mathrm{CgLp}}(\omega)-\arctan\left(\frac{\omega}{\omega_l}\right) = \arctan\left(\frac{b\omega_f^2-\omega_f(b\omega_l+a\omega)+(a-1)\omega\omega_l}{a\omega_f^2-\omega_f((a-1)\omega_l-b\omega)-b\omega\omega_l}\right). \quad (46)$$

We define

$$Q=\tan\left(\theta_{\mathrm{CgLp}}(\omega)-\arctan\left(\frac{\omega}{\omega_l}\right)\right) \quad (47)$$

which from (46) can be written as

$$Q=\left(\frac{b\omega_f^2-\omega_f(b\omega_l+a\omega)+(a-1)\omega\omega_l}{a\omega_f^2-\omega_f((a-1)\omega_l-b\omega)-b\omega\omega_l}\right). \quad (48)$$

Expanding (48) results in the following second-order equation:

$$(aQ-b)\omega_f^2+(b\omega Q+b\omega_l+a\omega-(a-1)\omega_l Q)\omega_f -\omega\omega_l(bQ+a-1)=0. \quad (49)$$

Solving the equality in (49) gives two values for ω_f as

$$\omega_{f_1}=\frac{-k_2-\sqrt{k_2^2-4k_1k_3}}{2k_1} \quad (50)$$

and

$$\omega_{f_2}=\frac{-k_2+\sqrt{k_2^2-4k_1k_3}}{2k_1} \quad (51)$$

where

$$\begin{aligned} k_1&=aQ-b\\ k_2&=b\omega Q+b\omega_l+a\omega-(a-1)\omega_l Q\\ k_3&=-\omega\omega_l[bQ+a-1]. \end{aligned} \quad (52)$$

Since we consider the required phase as $\theta_{\mathrm{CgLp}}(\omega)\in(0,\theta_M(\omega))$, it follows from Lemma 1 that there is at least one solution for $\omega_f\in[\omega_l,\infty)$ that satisfies the given phase requirement. The second solution for ω_f may lie either within or outside the interval $[\omega_l,\infty)$.

If two solutions exist within $[\omega_l,\infty)$, the smaller one is chosen, as terminating the nonlinear integrator action earlier reduces the impact of HOSIDFs. Conversely, if the second solution falls outside the interval $[\omega_l,\infty)$, $(\omega_f<\omega_l)$, the other solution $(\omega_f\geq\omega_l)$ is selected. This results in

$$\omega_f=\begin{cases}\min(\omega_{f_1},\omega_{f_2}), & \text{if both } \omega_{f_1},\omega_{f_2}\in[\omega_l,\infty)\\ \max(\omega_{f_1},\omega_{f_2}), & \text{otherwise.}\end{cases} \quad (53)$$

Please note that there always exists at least one real and positive solution for ω_f that results in a $\theta_{\mathrm{CgLp}}(\omega)<\theta_M(\omega)$ degree phase because any phase smaller than the maximum achievable phase $(\theta_M(\omega))$ is attainable. Consequently, when ω_{f_1} and ω_{f_2} are the only solutions, at least one of them is guaranteed to be real and positive.□

REFERENCES

[1] J. Freudenberg, R. Middleton, and A. Stefanpoulou, "A survey of inherent design limitations," in *Proc. Amer. Control Conf.*, Jun. 2000, pp. 2987–3001.

[2] M. M. Seron, J. H. Braslavsky, and G. C. Goodwin, *Fundamental Limitations in Filtering and Control*. Cham, Switzerland: Springer, 2012.

[3] B. Hunnekens, N. van de Wouw, M. Heertjes, and H. Nijmeijer, "Synthesis of variable gain integral controllers for linear motion systems," *IEEE Trans. Control Syst. Technol.*, vol. 23, no. 1, pp. 139–149, Jan. 2015.

[4] D. A. Deenen, M. F. Heertjes, W. P. M. H. Heemels, and H. Nijmeijer, "Hybrid integrator design for enhanced tracking in motion control," in *Proc. Amer. Control Conf. (ACC)*, May 2017, pp. 2863–2868.

[5] S. A. Hosseini, L. F. van Eijk, M. B. Kaczmarek, and S. H. HosseinNia, "Higher-order sinusoidal-input describing function analysis of fractional-order hybrid integrator-gain systems," *IFAC-PapersOnLine*, vol. 58, no. 7, pp. 400–405, 2024.

[6] A. Baños and A. Barreiro, *Reset Control Systems*. Cham, Switzerland: Springer, 2012.

[7] Y. Guo, L. Xie, and Y. Wang, *Analysis and Design of Reset Control Systems*. Savoy Place, London: Institution of Engineering and Technology, 2015.

[8] Y. Guo, Y. Wang, and L. Xie, "Frequency-domain properties of reset systems with application in hard-disk-drive systems," *IEEE Trans. Control Syst. Technol.*, vol. 17, no. 6, pp. 1446–1453, Nov. 2009.

[9] D. Caporale, L. F. van Eijk, N. Karbasizadeh, S. Beer, D. Kostic, and S. H. HosseinNia, "Practical implementation of a reset controller to improve performance of an industrial motion stage," *IEEE Trans. Control Syst. Technol.*, vol. 32, no. 4, pp. 1451–1462, Jul. 2024.

[10] H. K. Khalil, *Nonlinear Systems*, 3rd ed., Upper Saddle River, NJ, USA: Prentice-Hall, 2002.

[11] N. Saikumar, K. Heinen, and S. H. HosseinNia, "Loop-shaping for reset control systems: A higher-order sinusoidal-input describing functions approach," *Control Eng. Pract.*, vol. 111, Jan. 2021, Art. no. 104808.

[12] A. A. Dastjerdi, A. Astolfi, N. Saikumar, N. Karbasizadeh, D. Valerio, and S. H. HosseinNia, "Closed-loop frequency analysis of reset control systems," *IEEE Trans. Autom. Control*, vol. 68, no. 2, pp. 1146–1153, Feb. 2023.

[13] L. F. van Eijk, D. Kostic, M. Khosravi, and S. H. HosseinNia, "Higher order sinusoidal-input describing function analysis for a class of multiple-input multiple-output convergent systems," *IEEE Trans. Autom. Control*, vol. 70, no. 1, pp. 673–680, Jan. 2025.

[14] X. Zhang, M. B. Kaczmarek, and S. H. HosseinNia, "Frequency response analysis for reset control systems: Application to predict precision of motion systems," *Control Eng. Pract.*, vol. 152, Nov. 2024, Art. no. 106063. [Online]. Available: https://www.sciencedirect.com/science/article/pii/S0967066124002223

[15] J. C. Clegg, "A nonlinear integrator for servomechanisms," *Trans. Amer. Inst. Electr. Eng., II, Appl. Ind.*, vol. 77, no. 1, pp. 41–42, Mar. 1958.

[16] I. Horowitz and P. Rosenbaum, "Non-linear design for cost of feedback reduction in systems with large parameter uncertainty," *Int. J. Control*, vol. 21, no. 6, pp. 977–1001, Jun. 1975.

[17] L. Hazeleger, M. Heertjes, and H. Nijmeijer, "Second-order reset elements for stage control design," in *Proc. Amer. Control Conf. (ACC)*, Jul. 2016, pp. 2643–2648.

[18] N. Saikumar, R. K. Sinha, and S. H. HosseinNia, "'Constant in gain lead in phase' element-application in precision motion control," *IEEE/ASME Trans. Mechatronics*, vol. 24, no. 3, pp. 1176–1185, Mar. 2019.

[19] S. A. Hosseini and S. H. HosseinNia, "Frequency domain stability and convergence analysis for general reset control systems architecture," 2025, *arXiv:2502.09309*.
[20] G. Zhao, D. Nešić, Y. Tan, and C. Hua, "Overcoming overshoot performance limitations of linear systems with reset control," *Automatica*, vol. 101, pp. 27–35, Mar. 2019.
[21] N. Karbasizadeh, A. A. Dastjerdi, N. Saikumar, D. Valério, and S. H. Hossein Nia, "Benefiting from linear behaviour of a nonlinear reset-based element at certain frequencies," in *Proc. Austral. New Zealand Control Conf. (ANZCC)*, Nov. 2020, pp. 226–231.
[22] K. J. Åström and B. Wittenmark, *Computer-controlled Systems: Theory and Design*. North Chelmsford, MA, USA: Courier Corporation, 2013.
[23] L. F. van Eijk, Y. Liu, X. Zhang, D. Kostić, and S. H. HosseinNia, "A nonlinear integrator based on the first-order reset element," *IFAC-PapersOnLine*, vol. 58, no. 7, pp. 382–387, 2024.

S. Ali Hosseini received the M.Sc. degree in systems and control engineering, specializing in nonlinear control (with a focus on hybrid integrator-gain systems) from Sharif University of Technology, Tehran, Iran, in 2022. He is currently pursuing the Ph.D. degree with the Department of Precision and Microsystems Engineering, Delft University of Technology, Delft, The Netherlands.

His research focuses on addressing industrial control challenges using nonlinear control techniques in close collaboration with ASMPT, Beuningen, The Netherlands. His research interests include precision motion control, nonlinear control systems (such as reset and hybrid systems), and mechatronic system design.

Fabian R. Quinten received the M.Sc. degree in mechanical engineering with specialization in mechatronics from Delft University of Technology, Delft, The Netherlands, in 2024.

Luke F. van Eijk received the B.Sc. (cum laude) and M.Sc. (Hons.) degrees in mechanical engineering from Eindhoven University of Technology, Eindhoven, The Netherlands, in 2018 and 2021, respectively, with a focus on dynamics and control. He is currently pursuing the Ph.D. degree with the Department of Precision and Microsystems Engineering, Delft University of Technology, Delft, The Netherlands.

He is currently a Mechatronics Engineer at ASMPT, Beuningen, The Netherlands. His research interests include analysis and design of (non)linear feedback controllers, with a particular focus on reset control and the hybrid integrator-gain systems.

Dragan Kostić received the Ph.D. degree in control technology and robotics from Eindhoven University of Technology, Eindhoven, The Netherlands, in 2004.

His professional positions range from research and teaching at knowledge institutions to professional engineering in commercial companies. Multidisciplinary system modeling and identification, data-based controls, and nonlinear control designs are his main areas of expertise. He works at ASMPT, Beuningen, The Netherlands, as the Research and Development Director of mechatronics. His current research interests include modeling, dynamical analysis, and control of hi-tech mechatronic systems for semiconductor manufacturing.

S. Hassan HosseinNia (Senior Member, IEEE) received the Ph.D. degree (Hons. and cum laude) in electrical engineering specializing in automatic control: application in mechatronics from the University of Extremadura, Badajoz, Spain, in 2013.

Since October 2014, he has been appointed as a Faculty Member with the Department of Precision and Microsystems Engineering, Delft University of Technology, Delft, The Netherlands. He has an industrial background, having worked at ABB, Västerås, Sweden. He has co-authored numerous articles in respected journals, conference proceedings, and book chapters. His main research interests include precision mechatronic system design, precision motion control, and mechatronic systems with distributed actuation and sensing.

Dr. HosseinNia served as the General Chair for the 7th IEEE International Conference on Control, Mechatronics, and Automation (ICCMA 2019). He is currently an Editorial Board Member of *Fractional Calculus and Applied Analysis*, *Frontiers in Control Engineering*, and *International Journal of Advanced Robotic Systems (SAGE)*.